

# The Accretion History of the Milky Way: III. Hydrodynamical Simulations of Galactic Dwarf Galaxies at First Infall

Jianling Wang<sup>1,2\*</sup>, Francois Hammer<sup>1†</sup>, Yanbin Yang<sup>1</sup>, Marcel S. Pawlowski<sup>3</sup>, Gary A. Mamon<sup>4</sup>, Haifeng Wang<sup>5</sup>

<sup>1</sup>*GEPI, Observatoire de Paris, Paris Sciences et Lettres, CNRS, Place Jules Janssen 92195, Meudon, France.*

<sup>2</sup>*CAS Key Laboratory of Optical Astronomy, National Astronomical Observatories, Beijing 100101, China*

<sup>3</sup>*Leibniz-Institut fuer Astrophysik Potsdam (AIP), An der Sternwarte 16, D-14482 Potsdam Germany*

<sup>4</sup>*Institut d'Astrophysique de Paris (UMR7095: CNRS & Sorbonne Université), 98 bis Bd Arago, 75014, Paris, France*

<sup>5</sup>*CREAF, Centro Ricerche Enrico Fermi, Via Panisperna 89A, I-00184, Roma, Italy*

Received ; accepted

## ABSTRACT

Most Milky Way dwarf galaxies are much less bound to their host than are relics of Gaia-Sausage-Enceladus and Sgr. These dwarfs are expected to have fallen into the Galactic halo less than 3 Gyr ago, and will therefore have undergone no more than one full orbit. Here, we have performed hydrodynamical simulations of this process, assuming that their progenitors are gas-rich, rotation-supported dwarfs. We follow their transformation through interactions with the hot corona and gravitational field of the Galaxy. Our dedicated simulations reproduce the structural properties of three dwarf galaxies: Sculptor, Antlia II and, with somewhat a lower accuracy, Crater II. This includes reproducing their large velocity dispersions, which are caused by ram-pressure stripping and Galactic tidal shocks. Differences between dwarfs can be interpreted as due to different orbital paths, as well as to different initial conditions for their progenitor gas and stellar contents. However, we failed to suppress in a single orbit the rotational support of our Sculptor analog if it is fully dark-matter dominated. In addition, we have found that classical dwarf galaxies like Sculptor may have stellar cores sufficiently dense to survive the pericenter passage through adiabatic contraction. On the contrary, our Antlia II and Crater II analogs are tidally stripped, explaining their large sizes, extremely low surface brightnesses, and velocity dispersion. This modeling explains differences between dwarf galaxies by reproducing them as being at different stages of out-of-equilibrium stellar systems.

**Key words:** Galaxies: evolution - Galaxies: interactions - galaxies: dwarf - Galaxy: structure - Galaxy: halo

## 1 INTRODUCTION

The *Gaia* mission's measurements of the bulk proper motions of Milky Way (MW) dwarf galaxies have opened a new avenue to understand these low mass stellar systems. Hammer et al. (2023a, hereafter Paper I) established an empirical relation between the infall lookback time and the logarithm of the orbital energy by comparing the total orbital energy of dwarfs to that of events with well-known infall time (Gaia-Sausage-Enceladus, 8-10 Gyr, Sgr, 4-6 Gyr ago). This empirical relation is in excellent agreement with theoretical predictions from cosmological simulations (Rocha et al. 2012), and it suggests that most dwarfs arrived recently (< 3 Gyr ago). The late infall of dwarfs requires reconsidering<sup>1</sup> the properties of their progenitors outside the MW halo, which are likely gas-rich dwarf galaxies. This is because most dwarfs outside MW or M31 halos are dwarf irregulars (dIrrs) as shown by Putman et al. (2021), and their passage into the MW halo gas may have fully transformed

them (Mayer et al. 2006; Yang et al. 2014). This is expected because (1) of the considerable loss of mass associated to the gas removal through ram pressure from the MW halo gas (Yang et al. 2014), (2) the strong turbulence caused by this gas extraction affecting both gas and stellar kinematics, and (3) of Galactic tidal shocks (Hammer et al. 2023b, hereafter Paper II) mostly occurring at pericenter, a location close to which many dwarf galaxies are found (Fritz et al. 2018; Li et al. 2021).

The presence of a hot corona surrounding the MW is necessary to explain the dual HI filaments of the Magellanic Stream (e.g., Hammer et al. 2015; Wang et al. 2019), while the Leading Arm has been suggested to be generated by satellites moving ahead of the LMC (Tepper-García et al. 2019). This hot gas exerts ram-pressure on the dwarf progenitors and strip their gas. Other evidences for the presence of MW hot gas are coming from (1) the dichotomy of gas content in gas-poor (rich) dwarfs inside (outside) the MW or M31 halo (Grcevich & Putman 2009; Putman et al. 2021), and (2) the gaseous disk of the Large Magellanic Cloud (LMC) that has shrunk enough to be smaller than the stellar counterpart suggesting very strong ram-pressure effects (Nidever 2014; Salem et al. 2015), which make it rather unique among other dIrrs. Detection of the high velocity cloud

\* E-mail: wjianl@bao.ac.cn

† E-mail: francois.hammer@obspm.fr

<sup>1</sup> Otherwise, if dwarfs were accreted a long time ago, most of their progenitor properties would have been diluted during the numerous subsequent orbits that would have let enough time to reach equilibrium.

dissociations at distances larger than 50 kpc by Kalberla & Haud (2006) implies densities of few  $10^{-4} \text{ cm}^{-3}$ , which are consistent with all other estimates (Salem et al. 2015; Hammer et al. 2015; Wang et al. 2019; Putman et al. 2021).

The above paragraphs suggest that most dwarf properties result from a temporal sequence, beginning with gas stripping due to MW halo gas ram-pressure, expansion of their stars due to the subsequent lack of gravity, and then a significant impact of MW tidal shocks exerted mostly on the leaving stars. The impact of such an out-of-equilibrium process has been theoretically described by Hammer et al. (2023b hereafter Paper II). The latter shows that dwarf velocity dispersions are likely increased by gas turbulence, expansion of the stellar distribution and tidal shocks. It comes out that most MW dwarfs as they are observed today are not in equilibrium, and that the self-equilibrium conditions assumed by Walker et al. (2009) and Wolf et al. (2010) cannot be applied to them.

The goal of this paper is to verify whether one can reproduce through hydrodynamical simulations the properties of MW dwarf galaxies after assuming they are at their first infall in the MW halo. Section 2 describes the hydrodynamical model and the initial conditions for the MW and dwarf progenitors including their gas content (Section 2.3.2). Section 2.3.3 shows that we failed to reproduce a dispersion-supported Sculptor analog when its progenitor is dark-matter dominated. Section 3 shows the simulations of Sculptor, Antlia II and Crater II analogs, and compares the results to observations. The differences in size and velocity dispersion between these three dwarfs can be simply explained by their different orbital paths. Section 3 also investigates the numerical convergence issues, especially those related to the gas removal conditions. Section 4 discusses the different mechanisms that explains the different properties of the simulated dwarf galaxies together with predictions for future observations, while Section 5 summarizes the main results of the study.

## 2 HYDRODYNAMICAL MODEL AND INITIAL CONDITIONS FOR THE MILKY WAY AND DWARF PROGENITORS

### 2.1 Hydrodynamical model

Numerical simulations have been carried out with GIZMO (Hopkins 2015), which is based on a new Lagrangian method for hydrodynamics, and has simultaneously properties of both smoothed particle hydrodynamics (SPH) and grid-based/adaptive mesh refinement (AMR) methods. It has considerable advantages when compared to SPH: proper convergence, good capturing of fluid-mixing instabilities, dramatically reduced numerical viscosity, and sharp shock capturing. These features make GIZMO much more advanced to capture hydrodynamics than GADGET-2 (Springel 2005), which is unable to properly account for, e.g., Kelvin-Helmholtz instabilities.

### 2.2 Initial conditions for the Milky Way and its halo gas

The MW model is set up from that used in Wang et al. (2019), which reproduces well the Magellanic System including the Magellanic Stream, Clouds, and Bridge. Many predictions from this model have been confirmed by recent observations (Wang et al. 2022). Wang et al. (2019) used two similar MW models, which includes a stellar disc, gas disc, hot gas corona, and dark matter halo. The hot corona density profiles are slightly different in these two models, but both of them can reproduce well the Magellanic System (Wang et al. 2019).

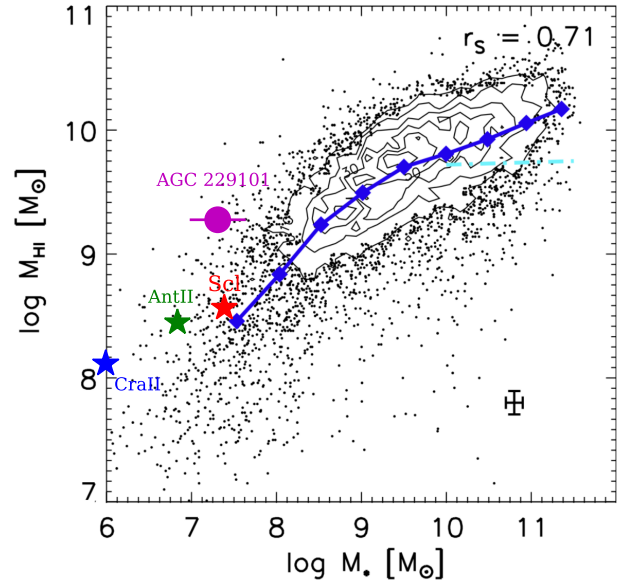


**Figure 1.** Stellar mass versus HI mass distribution for ALFALFA sample (black dots and contours) from Huang et al. (2012), to which we have added the progenitors of Crater II (blue star), Antlia II (green star), and Sculptor (red star). Blue diamonds and solid lines indicate the mean values in each stellar mass bin. The cyan dash-dotted line is the average value of the GASS galaxies with  $M_* \geq 10^{10} M_\odot$  from Catinella et al. (2010). The Spearman rank correlation coefficients ( $r_s$ , Huang et al. 2012) is labelled on the top right. The almost dark galaxy AGC 229101 from Leisman et al. (2021) is indicated by a magenta circle.

In this work, we adopt model MW1 of Wang et al. (2019), which has a total dynamical mass of  $6.8 \times 10^{11} M_\odot$  (see Wang et al. 2019 for details). The total number of particles in the MW model is around 30 million, for which masses of dark matter and corona gas particles are  $10^5 M_\odot$ .

### 2.3 Initial conditions for dwarf progenitors

#### 2.3.1 Preliminary investigations and stability of initial conditions

The progenitors of MW dwarf galaxies are assumed to be gas-rich dwarfs, and they include a rotationally-dominated, thick-disk stellar component and a disk gas component. In this paper, we initially focus on reproducing the properties of the Sculptor dwarf spheroidal galaxy (dSph) that is ranked the third in mass among classical dSphs, which also helps to keep a reasonable mass ratio between MW halo gas particles and dwarf gas particles ( $m=10^4 M_\odot$ ). Sculptor is an interesting dSph to study because it has been often considered as an archetype for an ancient satellite of the MW, due to its old stellar population (de Boer et al. 2012). During our preliminary tests, we have found that a single stellar component is very fragile to the gas loss and to Galactic tidal shocks. It results in a very low surface brightness remnant, reminiscent of Antlia II and Crater II. Therefore, we have added a cored stellar component with an exponential profile for the Sculptor progenitor, which has a stellar mass of  $5 \times 10^6 M_\odot$  together with a half mass radius of 0.15 kpc (see Table 1). This is consistent with the WLM dwarf stellar-density profile, whose thick disk requires two Sersic profiles to be reproduced (Higgs et al. 2021).

**Table 1.** Initial condition parameters and particle numbers for the progenitors of three Galactic dwarfs.

Dwarf Model	DM-dominated Sculptor	Sculptor	Antlia II	Crater II
Gas disc mass ( $10^8 M_\odot$ )	0.3	6.0	4.5	2.0
Stellar component mass ( $10^6 M_\odot$ )	5	20.	7.0	1.0
Stellar core mass ( $10^6 M_\odot$ )	–	5.	–	–
Scale radius of gas Disk (kpc)	0.56	1.5	2.0	2.0
Projected effective radius of stellar component (kpc)	0.279	0.5	0.5	0.3
Sersic index ( $n$ ) of stellar component	1	0.5	1.0	0.77
Axis ratio of stellar component	0.6	0.6	1.0	1.0
Number of Stellar Particles	3000	12000	7500	6000
Number of Gas Particles	3000	60000	68000	60000

Here, we have not considered reproducing dwarfs less massive in stars, including 10 times smaller dSphs such as UMi, Draco or Carina, or even ultra-faint dwarfs, because it would have led to uncomfortably high mass ratios of MW halo gas to dwarf gas particles (see Section 3.5). Initial conditions have been created with a Schwarzschild orbit superposition method (Vasiliev 2013, 2019). To test the stability of the initial conditions, we have let the dwarf progenitors evolve in isolation for 2 Gyr. Figure A1 of Appendix A shows the time evolution of the projected stellar surface mass density and of the projected velocity dispersion profiles. Their cores are mostly preserved during their evolution in isolation, although their outskirts are affected especially by feedback processes, which does not affect our simulation results when launching them to interact with the MW halo and its corona.

### 2.3.2 Stellar and gas mass of the progenitors

Huang et al. (2012) compared the HI mass versus stellar mass relation for local galaxies (see Figure 1). They found that many field dwarfs are gas-dominated, with stellar mass ranging from  $10^6 M_\odot$  to  $2 \times 10^8 M_\odot$ , and HI gas mass ranging from  $10^8 M_\odot$  to  $10^{10} M_\odot$ .

We have used the average values of local galaxies (see Figure 1) to capture the properties of the Sculptor progenitor. However, we notice that gas-rich dwarfs lost a significant part of their stellar content during their infall and gas-stripping. This is because after gas exhaustion, the stellar content expands due to the related lack of gravity and it becomes easily affected by MW tides (see description in Paper II). We have then chosen the Sculptor progenitor with a stellar mass of  $2.5 \times 10^7 M_\odot$ <sup>2</sup>, leading to an HI mass  $M_{\text{HI}} = 6 \times 10^8 M_\odot$  (see Table 1), if it follows the  $M_{\text{HI}}-M_{\text{stars}}$  relation of Figure 1. The progenitor of Sculptor is then assumed to have a 96% gas fraction (see Table 1). This is comparable to that of the NGC 3109 dwarf. The latter has a stellar mass of  $7.6 \times 10^7 M_\odot$ , and a HI mass of  $4.5 \times 10^8 M_\odot$  (McConnachie 2012), which corresponds to a 90% gas fraction when accounting for Helium.

Given our promising preliminary tests, we have also tried to reproduce Antlia II and Crater II with a single stellar component.

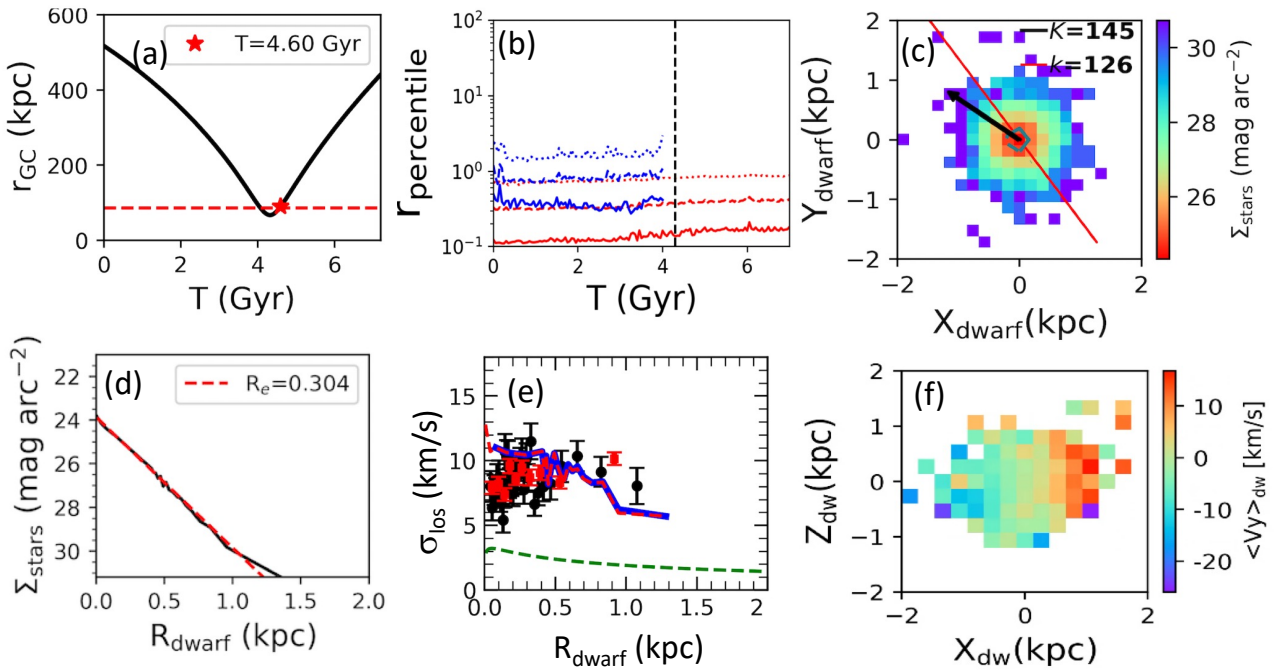
They possess stellar masses approximately 10 times smaller than that of Sculptor. We have considered the possibility of an extremely large gas fraction for the progenitors of Antlia II and Crater II, which would strongly impact their stellar content after the gas has been removed by ram pressure. We have then assumed 99.5% and 98.5% for the gas fraction of Antlia II and Crater II progenitors, respectively (see Table 1). Such very high gas fraction has been found by Leisman et al. (2021) when analyzing the unusual HI-dominated galaxy, AGC229101, which has been observed with the Arecibo Legacy Fast ALFA (ALFALFA). Its HI mass is  $10^{9.31 \pm 0.05} M_\odot$  with a stellar mass of  $10^{7.32 \pm 0.33} M_\odot$ , which leads to a neutral gas fraction of 98%, a value quite similar to that of Coma P (Leisman et al. 2021).

Figure 1 compares the distribution of stellar mass and HI mass of our dwarf progenitors with that of observed local galaxies. It indicates that the Sculptor progenitor lies well in the expected region for a galaxy with that stellar mass, while Antlia II and especially Crater II progenitors, are on the high-gas fraction side of the distribution, together with AGC229101. Table 1 lists the progenitor properties of Antlia II and Crater II. Progenitors of Antlia II and Crater II are more exceptional than that of Sculptor, consistent with the fact that the latter is more representative of MW dwarf galaxies than the former two dwarfs (Ji et al. 2021).

### 2.3.3 The role of dark matter and constraints on its content in the Sculptor progenitor

MW dSph galaxies have been considered to be dark-matter (DM) dominated, assuming that their large velocity dispersions are due to equilibrium with their total mass (Walker et al. 2009; Wolf et al. 2010). This scenario is consistent with a very early infall of their gas-rich and rotationally-supported progenitors, offering a very large elapsed time during which they can be transformed into dispersion-supported dSphs (Mayer et al. 2006). Conversely to that, the large orbital energy of dwarf galaxies when it is compared to that of Sgr or GSE relics, suggests that they come recently, less than 3 Gyr ago, to our neighborhood. In such a case, one has to test whether a Sculptor progenitor that is rotating and DM dominated could be transformed into a dwarf spheroidal within less than one orbit. We have adopted a total mass derived from Wolf et al. (2010, see their Equation 2) with  $\sigma_{\text{los}} = 9.2 \text{ km s}^{-1}$ , which leads to  $2.2 \times 10^7 M_\odot$  within a 279 pc

<sup>2</sup> However, during our test of dark matter properties (see Section 2.3.3, we have also used stellar mass of  $5 \times 10^6 M_\odot$ , i.e., that of the Sculptor dSph.



**Figure 2.** Simulation model of a dark matter-dominated, gas-rich dwarf infall into the Galactic corona, with the gas being removed close to pericenter. This model has the goal to reproduce the Sculptor dwarf after assuming that its progenitor is embedded into a massive dark matter halo with a mass calculated from (Wolf et al. 2010). Panel (a): The orbital history of the simulated dwarf (black line), for which the red star indicates the present-day dwarf position. At this time, the gas has been stripped by ram-pressure. Panel (b): Evolution of the radii containing 10% (solid line), 50% (dashed line) and 90% (dotted-line) of the total mass, respectively. Red (blue) lines indicate the stellar (gas) component, respectively. The vertical line indicates the time at pericenter passage. Panel (c): Surface brightness profile overlapping contours showing the stellar shape of the dwarf. The red line shows the major axis. The black arrow indicates the proper motion direction, which is 19 degrees offset from the major axis. Panel (d): The black line shows the stellar surface brightness profile assuming  $M_{\text{stars}}/L_V = 2.5$ , while the dashed red line indicates an exponential profile fitting the central region (half-light radius value is indicated on the top-right of the panel). Panel (e): Radial velocity dispersion distribution as a function of the radius. The blue line shows the measured values, while the red-dashed line shows results after subtracting the radial velocity gradient as it is done for observed quantities (Walker et al. 2009). The dashed green line shows the contribution to the radial velocity dispersion that is due to the gravity of the single stellar mass. The observed velocity dispersions at different radii are shown by solid black circles for Walker et al. (2009) and with red dots for Iorio et al. (2019) observations, respectively. Panel (f): It shows the dwarf as it would be seen edge-on to illustrate its mean velocity along the Y direction, showing a significant rotational gradient that is much larger than that observed in Sculptor.

half-light radius<sup>3</sup>. Extrapolating it to large radii, Read et al. (2019) calculated a halo mass of  $5.7 \times 10^9 M_{\odot}$ . We have also adopted the orbital parameters of Sculptor, that are discussed in Section 3.1. This has resulted in a DM gravity being sufficiently large to prevent any gas removal during the first passage and up to the present-day Sculptor position.

To investigate under which conditions the gas can be removed after a single pericenter passage, we have then considerably diluted the gas in the progenitor by dividing its mass by a factor 10 while keeping the same scaling (see Table 1). However, this second model was not predictive of the observed stellar mass, because the DM component is sufficiently massive to shield the stellar component that is mostly preserved. This has prompted us to consider a third DM-dominated progenitor, with an initial stellar mass of  $5 \times 10^6 M_{\odot}$  (i.e., that of the Sculptor dwarf) that follows an exponential profile with a half mass radius of 0.279 kpc. The gas fraction (85%) has been adopted following the observational constraint from Figure 1. The gas component has been assumed with a scalelength 3 times larger than that of the stellar component. In the third model, the gas

is removed near pericenter (see panels (a) and (b) of Figure 2), and becomes rapidly ionized since it was already heated in the dwarf due to the strong DM gravity, explaining why no more neutral gas appears in panel (b) at  $T > 4$  Gyr.

Panel (b) also shows that the stellar component stays almost untouched during the whole simulation, which is confirmed by panel (d) showing a surface brightness profile very similar to the initial one (same exponential profile and half-light radius). Panel (e) provides the velocity dispersion radial profile, which is likely due to the internal equilibrium with the total mass as it has been assumed from Equation 2 of Wolf et al. (2010). It implies that most properties of Sculptor are reproduced this way, simply because the stellar content and its velocity dispersion stayed untouched because they were shielded by the dominant DM component.

However, panel (f) indicates a significant rotation pattern (rotational velocity larger than  $10 \text{ km s}^{-1}$ ), after placing the dwarf edge-on, conversely to observations that show Sculptor kinematics fully dominated by velocity dispersion (and a velocity gradient smaller than a few  $\text{km s}^{-1}$ , see Section 3.2). We have not been able to find a DM-dominated Sculptor progenitor that would be consistent with the present-day Sculptor kinematics, as well as with the presence of stars in the very outskirts of dwarfs. This is because a dominant DM component always shields the stellar component and its kinematics against perturbation due to gas loss

<sup>3</sup> We have adopted a NFW model (Navarro et al. 1997) for the dSph, and in our third model shown in Figure 2, the number and mass of dark matter particles are  $10^6$  and  $5023 M_{\odot}$ , respectively.



and Galactic tides. This is in agreement with simulations made by Mayer et al. (2006) who found that several orbits are necessary to successfully realize a transformation from a rotation-supported to a dispersion-supported stellar system. It does not mean that MW dwarfs do not possess DM, but simply that a recent infall dramatically reduces the parameter space against large amounts of DM.

Moreover, we notice that panel (a) of Figure 2 indicates a very large apocenter in excess of 400 kpc, or in other words that the dwarf has not been captured by the MW gravitational potential. Given the total mass of the MW adopted in our modeling ( $6.8 \times 10^{11} M_{\odot}$ , see Section 2.2) conversely to *Gaia* EDR3 measurements from Li et al. (2021) that indicates apocenter values between 133 to 209 kpc. In fact, in a DM-dominated dwarf, gas-removal becomes an almost negligible event, which prevents any slowdown associated to the gas removal. In addition, if dwarfs are DM-dominated dwarfs, the anti-correlation between DM density and pericenter may be difficult to understand, while it is predicted if they are out of equilibrium (see Paper II). Indeed, this is because the DM density may not have suffered from the Galactic tidal field during less than a single orbit (Cardona-Barrero et al. 2023, see their discussion section).

It is beyond the scope of this paper to search for the maximal amount of DM in the Sculptor progenitor to allow a full transformation of its kinematics, because it would require many additional simulations. We noticed that most of the DM content (about 70%) is not removed from the dwarf after a first passage at pericenter (Mayer 2010, see their Figure 1). Such a DM removal by Galactic tides is much less efficient than the ram pressure effect on gas that is fully removed. During our simulations of DM-free progenitors, we have noticed that if the initial gas component is more than twice the stellar component within the effective radius, it is sufficient to fully transform the dwarf kinematics after a single pericenter passage. Applying this to the combination of stellar and DM components, it implies an initial DM mass that has to be smaller than the initial gas mass within an effective radius of 279 pc, which is  $6.4 \times 10^5 M_{\odot}$  i.e., much smaller than  $2.2 \times 10^7 M_{\odot}$  within a 279 pc half-light radius of Sculptor.

As a consequence, we have followed Paper II that indicates the difficulty to estimate a dark matter content in dwarf galaxies out of equilibrium. In our models, progenitors of MW dwarfs have been assumed to be made by just a combination of gas and stars, with the goal to verify whether this is sufficient to explain the observations of the three dwarf galaxies considered here. One may also wonder why dIrrs that are known to contain a dominant DM component can be progenitors of dSphs such as Sculptor. This has been investigated by Hammer et al. (2019, see their Section 5.2) who found that only half of dIrrs selected from *Spitzer Photometry and Accurate Rotation Curves* (SPARC, Lelli et al. 2016) show evidence for a DM dominant component.

### 3 SIMULATIONS OF GAS-RICH DWARFS FALLING INTO THE MILKY WAY HALO

#### 3.1 Orbits of dwarf progenitors

Besides Sculptor that characterizes most dSphs well, the discovery of Antlia II (Torrealba et al. 2019) and Crater II (Torrealba et al. 2016) have prompted many questions in the Local Group community. Why do these galaxies have sizes comparable to that of the LMC, while their stellar masses are about 10, 000 times smaller?

Why do their DM densities appear to be significantly smaller than that of most dwarfs (Ji et al. 2021; Hayashi et al. 2023)? Our simulation resolution is unable to reach very low mass dSphs or ultra-faint dwarfs (see Section 2), but we verify during our preliminary simulations that both Antlia II and Crater II may have similar progenitors as Sculptor, after only changing the gas to stellar mass ratio.

We have generated the orbits for three dwarf galaxies following the *Gaia* DR3 proper motions calculated for different MW mass profiles by Li et al. (2021, see also Pace et al. 2022). From the high mass to the low mass MW model, the pericenters may vary from 54 kpc to 73 kpc (Sculptor), 56 kpc to 102 kpc (Antlia II), and 33 kpc to 58 kpc (Crater II), respectively. Another difficulty in calculating precise orbits is coming from the loss of orbital energy caused by ram pressure exerted on the dwarf before gas exhaustion.

To simplify the following simulations, we have used roughly the same orbital pericenter for the three dwarfs using values from 50 to 53 kpc. This is because our goal is not to reproduce in exquisite details the observed dwarfs, as this would need considerable efforts in fine tuning. Instead, our simulations have the goal to verify whether the physical mechanisms (ram-pressure resulting in gas loss, subsequent lack of gravity, and then tidal shocks) may explain the properties of dwarfs with large velocity dispersions, from dSphs (e.g., Sculptor) to unusual ultra-faint dwarfs such as Crater II and Antlia II. To reproduce the on-sky location of the dwarfs, we have carefully rotated each simulated system to the orbital plane of the observed corresponding dwarf, in order to match the snapshot sufficiently close to the observed sky position. During this rotation, we ignore the effect of Galactic disk on the dwarf orbital evolution, since the dwarf pericenters are much larger than the disk size.

Using the above methodology, simulated dwarfs will have positions and velocities that roughly match that from observations. In the following analyses, we have defined coordinate systems centered on each dwarf with orthographic projection in the sky as they are defined from observations (Gaia Collaboration et al. 2021). To compare with observations (Li et al. 2021), we have used the Galactic radial velocity which automatically remove the effect of solar reflex motion. Table 2 summarizes the comparison with observations, which are described in the three next sections. It includes comparison of orbital quantities and of structural properties. Given the large number of parameters, we cannot expect a perfect match that also change with the choice of the precise epoch. However, it can help us to identify methods for improving the modeling, e.g., by adapting the 3D velocity of the simulated Crater II (see discussion in Sect. 4.4). Comparison of the 3 simulated dwarf to observations are shown in Table 2.

#### 3.2 Modeling the Sculptor dSph properties

Sculptor is a classical dSph whose properties are reproduced in Figure 3 by our simulations. Panel (a) indicates that the dwarf is just 350 Myr after pericenter, at 83 kpc from the Galactic center, with a position on the sky similar to that observed (see Table 2).

Panel (b) of Figure 3 shows how the gas and stellar radii evolve with time. It gives the time evolution of radii including different fractions of gas mass (blue lines) or of stellar mass (red lines), respectively. Dotted, dashed, solid lines correspond to radii including 90%, 50%, 10% of gas/stellar mass, respectively. At pericenter ( $T \sim 4.5$  Gyr), the gas radius expands rapidly, which indicates that ram-pressure is efficient enough to strip the gas. The dwarf exhausts its gas 250 Myr later, and then stars are rapidly expanding (see red

**Table 2.** Comparison between modeling results with observations (references are in the last column).References: (1) Li et al. (2021); (2) Ji et al. (2021); (3) Muñoz et al. (2018); (4) Bettinelli et al. (2019); (5) Martínez-García et al. (2023); (6) Iorio et al. (2019). <sup>a</sup> Exponential stellar mass is that derived from the single exponential profile, which would neglect the faint additional component at large radii shown in panels (f) of Figures 3, 5, and 6. <sup>b</sup> The velocity dispersion measured for Sculptor analog is  $\sigma_{1\sigma_s}$ , and  $\sigma_{\text{gsr}}$  for Antlia II and Crater II analogs.

Parameters	Symbol	Units	Sculptor		Antlia II		Crater II		Refs
			Obs.	Model	Obs.	Model	Obs.	Model	
Ra	$\alpha$	deg	15.0183	14.8570	143.8079	143.4475	177.310	178.0151	(1),(2)
Dec	$\delta$	deg	-33.7186	-33.8081	-36.6991	-36.4327	-18.413	-18.7613	(1),(2)
Galactic radial velocity	$V_{\text{gsr}}$	$\text{km s}^{-1}$	$75.9^{+0.7}_{-7.0}$	115	$49.9^{+0.4}_{-0.4}$	102	$-81.4^{+0.3}_{-0.3}$	-172	(1),(2)
3D velocity	$V_{3\text{D}}$	$\text{km s}^{-1}$	$179.6^{+8.3}_{-8.3}$	202.2	$136.9^{+11.7}_{-11.7}$	142.6	$124.2^{+12.6}_{-12.1}$	241.8	(1),(2)
eccentricity	ecc		0.37 - 0.52	0.55	0.41 - 0.50	0.72	0.58 - 0.60	0.85	(1),(2)
Helio-distance	$d_{\odot}$	kpc	86	83	131.8	148	117.5	100	(1),(2)
Effective radius	$R_e$	kpc	0.311	0.29	2.54	3.98	1.07	1.05	(3),(2)
Exponential stellar mass <sup>a</sup>	$M_{\star}$	$10^6 M_{\odot}$	5.1	4.27	1.89	6.9	0.4	0.72	(4),(2)
Radial velocity gradient	$k_v$	$\text{km s}^{-1} \text{kpc}^{-1}$	$\sim 0.76$	0.5	2.49	1.3	1.07	0.7	(5),(2)
Velocity dispersion <sup>b</sup>	$\sigma_{1\sigma_s}$	$\text{km s}^{-1}$	8.9	$\sim 6.8$	5.98	$\sim 6$	2.34	$\sim 2.5$	(6),(2)

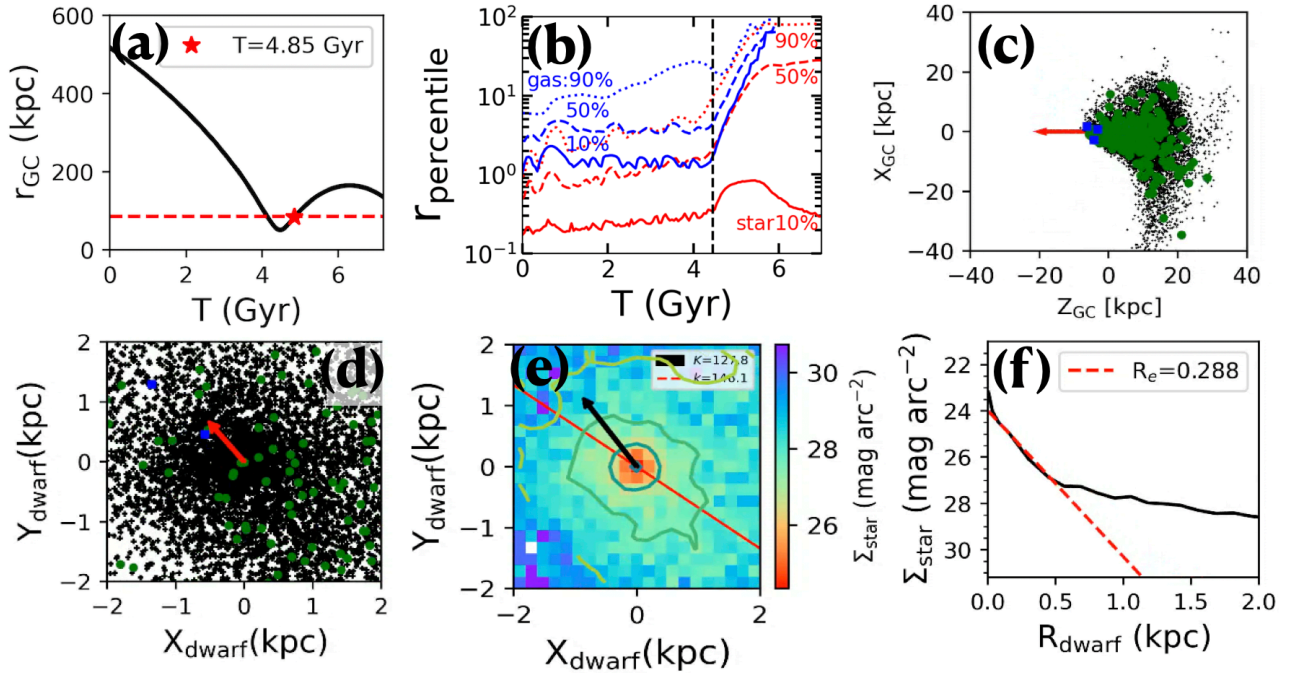


**Figure 3.** Simulation model of a gas-rich dwarf infall into Galactic corona, with the gas being removed close to pericenter. This model reproduces the Sculptor dwarf. Panel (a): The orbital history of the simulated dwarf (black line), for which the red star indicates the present-day dwarf position. At this time, the gas has been stripped by ram-pressure. Panel (b): Evolution of the radii containing 10% (solid line), 50% (dashed line) and 90% (dotted-line) of the total mass, respectively. Red (blue) lines indicate the stellar (gas) component, respectively. The vertical line indicates the time at pericenter passage. Panel (c): Stellar particle distribution in the orbital plane, for which the Z axis is pointing toward to the Galactic center (see the red arrow). Panel (d): Star particle distribution on sky. The red arrow indicates the proper motion direction. Green dots indicate stars that have been formed during the simulation, while the two magenta dots identify very young stars formed 0.5 Gyr ago. Panel (e): Surface brightness profile overlapping contours showing the stellar shape of the dwarf. The red line shows the major axis. The black arrow indicates the proper motion direction, which is 18.3 degrees offset from the major axis. Panel (f): The black line shows the stellar surface brightness profile assuming  $M_{\text{stars}}/L_V = 2.5$ , while the dashed red line indicates an exponential profile fitting the central region (half-light radius value is indicated on the top-right of the panel).

lines). In the meantime, tidal shocks at pericenter inject energy into the expanding stellar system controlling its 3D motion. Their impact is to accumulate stars along the line of sight (see panel c), which is also the direction of the MW gravity vector (see also Eq. 11 of Paper II). Both gas loss and tidal shocks boost the velocity dispersion, the former because stars kept their initial velocity dispersion enhanced by the initial gas gravity. MW tides strongly stretch the object at large scales. Besides this, stars in the central part of the dwarf move sufficiently fast that they are adiabatically invariant to the action of

MW tides, and they present an almost round distribution as indicated by panels (d, e), without evidence for tidal stripping signatures as it is observed within  $\Sigma_{\text{stars}} < 28 \text{ mag arcsec}^{-2}$ .

Panel (e) indicates a 18.3 degree offset between the proper motion direction and the major axis. The position angle (PA) of Sculptor is 94 degree (McConnachie & Venn 2020). The proper motion direction after correcting the solar reflex motion can be derived from *Gaia* EDR3 (Li et al. 2021). The observed difference between the

PA and proper motion direction is 56.8 degree, which corresponds to a higher misalignment than in our simulation.

Panel (f) shows the surface brightness distribution assuming a stellar mass to  $V$ -luminosity ratio of 2.5. The red-dashed line indicates the exponential function that fits the central region, and this gives a half-light radius of 0.29 kpc, which is consistent with that observed (0.279 kpc, see Muñoz et al. 2018). There is an additional component at the simulated Sculptor outskirts as it is indicated by the black line, which is consistent with the break observed by Westfall et al. (2006, see also Yang et al. 2022b). Sestito et al. (2023) found that the surface number density of Sculptor starts to deviate from exponential with an extra component at  $R > 0.8$  kpc, which is roughly consistent with our simulation ( $R > 0.5$  kpc).

Fourth row-left panel of Figure 4 shows a weak velocity gradient in the central region, which could be consistent with the small radial velocity gradient (see Table 2) observed within a central area of  $\sim 0.73$  kpc, or  $\sim 0.5$  degree (Martínez-García et al. 2023, see their Figure 4). However, the observed velocity gradient might be larger at the outskirts ( $\sim 5$  km s $^{-1}$  kpc $^{-1}$ , after accounting for the two points at both outskirts of Figure 1 of Battaglia et al. 2008), which are not reproduced by our simulations.

Top-left panel of Figure 4 shows the simulated velocity dispersion profile compared to that observed, with black and red points representing the observations from Walker et al. (2009) and from Iorio et al. (2019), respectively. The simulated velocity profile matches well the observed value, except in the very inner central part of the dwarf, where the velocity dispersion drops to lower values than that observed. To check how much velocity dispersion is contributed by the stellar mass component, we have built a stellar model with projected surface mass distribution following an exponential function based on panel (f) of Figure 3. By assuming an isotropic velocity dispersion caused by the stellar mass, we can derive the line of sight velocity dispersion against the radius, which is shown by the green dashed line in the top-left panel of Figure 4. The stellar mass contribution to the velocity dispersion is much lower than that observed. Consequently, gas removal and tidal shocks are responsible for the observed large velocity dispersion, and this stands for a duration of about 0.35 Gyr.

Panel (d) of Figure 3 shows the on-sky stellar particles distribution. Magenta points identify very young stars (age less than 0.5 Gyr), which have been formed just before the gas removal. They are also shown in panel (c) together with green points that represents stars formed during the whole simulation. Strong ram-pressure compress the gas before removing it, which helps to form new stars.

The third row-left panel of Figure 4 is based on Eq. 8 and Figure 5 of Paper II, i.e., the relation between  $\sigma_{\text{los}}^2/r_{\text{half}}^2$  and the strength of the tidal effect at pericenter :

$$\frac{\sigma^2}{r_{\text{half}}^2} = \frac{128}{27} \left( \frac{g_{\text{MW}}(R_{\text{peri}})}{V_{\text{peri}}} \right)^2, \quad (1)$$

where  $g_{\text{MW}}(R_{\text{peri}}) = GM_{\text{MW}}(R_{\text{peri}})/R_{\text{peri}}^2$  is the gravitational acceleration exerted by the assumed spherical MW at  $R_{\text{peri}}$ . Objects for which the right term of Eq. 1 dominates are known to be tidally stripped (e.g., Sgr and Pal 5, see Figure 5 in Paper II). The simulated Sculptor is above the line, which is consistent with its observed value in Paper II (see their Figure 5).

### 3.3 Modeling the Antlia II dwarf galaxy properties

Antlia II is the only MW dwarf galaxy that has been discovered using *Gaia* DR2 proper motions (Torrealba et al. 2019). It possesses a very large radius ( $r_{\text{half}} = 2.54$  kpc), an extremely low surface

brightness even when compared to the most ultra-faint dwarfs, and an ellipticity of 0.6. Its velocity dispersion is 5.98 km s $^{-1}$ , and it shows a large radial velocity gradient (2.49 km s $^{-1}$  kpc $^{-1}$ ).

Antlia II has a positive Galactic radial velocity (Li et al. 2021; Ji et al. 2021) and is leaving its pericenter toward its apocenter. Figure 5 shows the simulated properties of our modeled Antlia II, which appear quite similar to that of the observed Antlia II.

Panel (a) of Figure 5 shows the orbital evolution of the dwarf progenitor during its infall into the Galactic halo. Antlia II has lost its gas at pericenter passage ( $T_{\text{peri}} = 4.85$  Gyr, see Panel b), 0.65 Gyr before its present location (see the red star) at 143 kpc from the Galactic center, which is comparable to the observed value (132 kpc, Ji et al. 2021). Panels (c) and (d) shows the stellar particle distribution, for which green dots indicate the stars formed after the beginning of the simulation. Table 2 indicates that the dwarf is roughly at its current observed position.

Since the simulated Antlia II has left its pericenter where it has suffered strong tidal shocks and gas stripping, the dwarf has been stretched as shown by the elongated morphology in Panels (c), (d), and (e). In panel (e), the major axis (red line) and the proper motion direction (black arrow, after correcting the solar reflex motion) shares roughly the same direction with a difference of  $\sim 5$  degrees, which is comparable to the observational value ( $\sim 15$  degrees from Ji et al. 2021).

Fourth row-middle panel of Figure 4 shows the line-of-sight velocity distribution that is projected on sky. There is a significant velocity gradient of  $\sim 1.3$  km s $^{-1}$  kpc $^{-1}$  along the major axis, which is comparable but a bit smaller than the observed value (2.49 km s $^{-1}$  kpc $^{-1}$ , Ji et al. 2021).

Gas loss leads to an expansion of the stellar component, while Galactic tides strongly stretch the simulated dwarf along the orbital direction, as it is illustrated in Panels (c) and (d). Panel (f) shows the surface brightness profile after assuming a stellar mass to light ratio of 2.5. The simulated central surface-brightness is very low ( $\Sigma_{\text{stars}} \geq 29$  mag arcsec $^{-2}$ ), and consistent with the observed value within the half-light radius (30.7 mag arc $^{-2}$ , Ji et al. 2021). The half light radius is  $\sim 4$  kpc after fitting the profile with an exponential law. It is slightly larger than that observed, for which the major axis radius is around 4 kpc (Ji et al. 2021). Third row-middle panel of Figure 4 strongly supports the presence of strong tidal shocks and stripping since both the simulated and the observed Antlia II are found with a dominant right-term of Eq. 1, i.e., well below the dashed red line (see also Figure 5 of Paper II).

The top-middle panel of Figure 4 shows the radial profile of the velocity dispersion. The blue line shows the velocity dispersion as a function of radius. The red-dashed line indicates the velocity dispersion after removing the velocity gradient, as it is done in the analysis of the observations (Ji et al. 2021). It shows a velocity dispersion between 5 and 7 kms $^{-1}$ , which is comparable to the observed value for Antlia II (5.98 km s $^{-1}$ , Ji et al. 2021).

### 3.4 Modeling the Crater II dwarf galaxy properties

Crater II is located at  $\sim 117$  kpc, and it shows an extended structure with a half-light radius of  $\sim 1$  kpc, and a stellar mass of  $\sim 3.5 \times 10^5 M_{\odot}$  (Ji et al. 2021). Crater II is considered to be difficult to interpret because of its low velocity dispersion ( $\sim 2.3$  km s $^{-1}$ ), especially when it is compared to dwarfs with similar stellar mass.

In our simulation, the Crater II progenitor has lost its gas content well before pericenter passage. Panel (b) of Figure 6 shows how the gas and stellar radii evolve with time. The sizes of both gas and stellar components rapidly increase during the dwarf infall into the



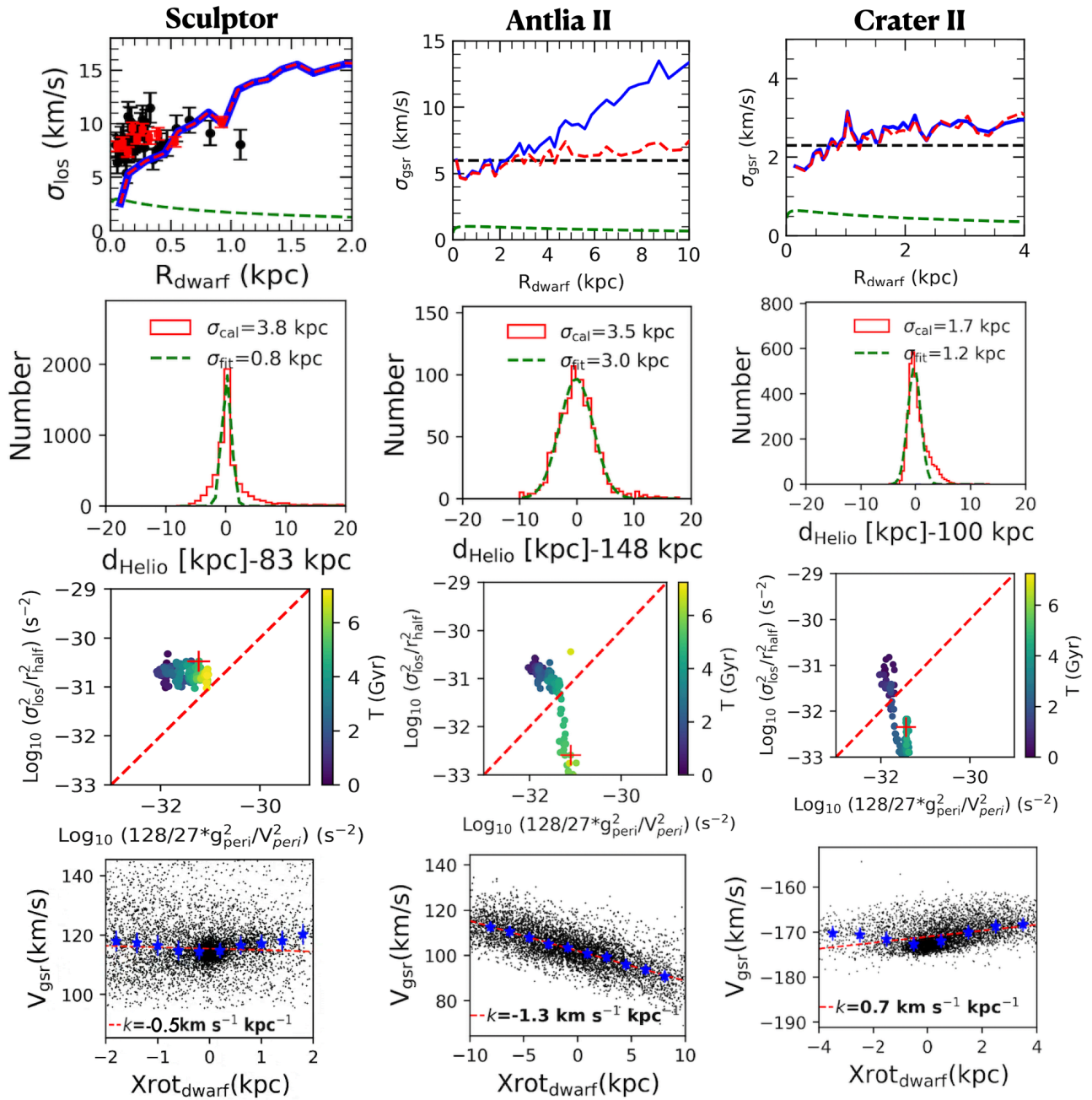


**Figure 4.** Kinematics properties of the 3 dwarf galaxies, Sculptor (first column), Antlia II (second column) and Crater II (third column). Top panels: Radial velocity dispersion distribution as a function of the radius. The blue line shows the measured values, while the red-dashed line shows results after subtracting the radial velocity gradient as it is done for observed quantities (Walker et al. 2009). The dashed green line shows the contribution to the radial velocity dispersion that is due to the stellar mass (see text). For Sculptor, the observed velocity dispersions at different radii are shown by solid black circles for Walker et al. (2009) and with red dots for Iorio et al. (2019) observations, respectively. Second-row panels: Simulated histogram for the distribution of stellar distances (minus the average distance of the dwarf) for stars selected within a 2 kpc radius. Third-row panels: The relation between  $\sigma_{\text{los}}^2/r_{\text{half}}^2$  and the theoretical value for tidal shocks as it is described in Eq. 1 (red-dashed line indicate the equality for which tidal shocks provide to the dwarf an energy equals to its binding energy). Red cross represents the present-day position of the dwarf and colored points indicate its evolution during the whole simulation. Fourth-row panels: Radial velocity distribution along the major axis. The blue stars and error bars indicate the median values and their uncertainties. The red line shows the gradient value that is given in the bottom left.

MW halo, due to the gas removal caused by ram-pressure. At  $T \sim 3.3$  Gyr, only 10% of gas remains within a 10 kpc radius, and none within a 4 kpc radius, which indicates that the gas has been fully removed from the dwarf core. This shows a very efficient gas stripping because of the shallow gravitational potential adopted for the Crater II progenitor.

Gas loss is accompanied by a gravity loss that makes the stellar component expand, as indicated by the red lines of panel (b) of Figure 6. At  $T=4.05$  Gyr, the dwarf arrives at  $\sim 100$  kpc from the Sun, with a on-sky position that is roughly consistent with that observed (see Table 2). Due to its expansion, the stellar component becomes very extended with a half-mass radius of  $\sim 1$  kpc according to the fit



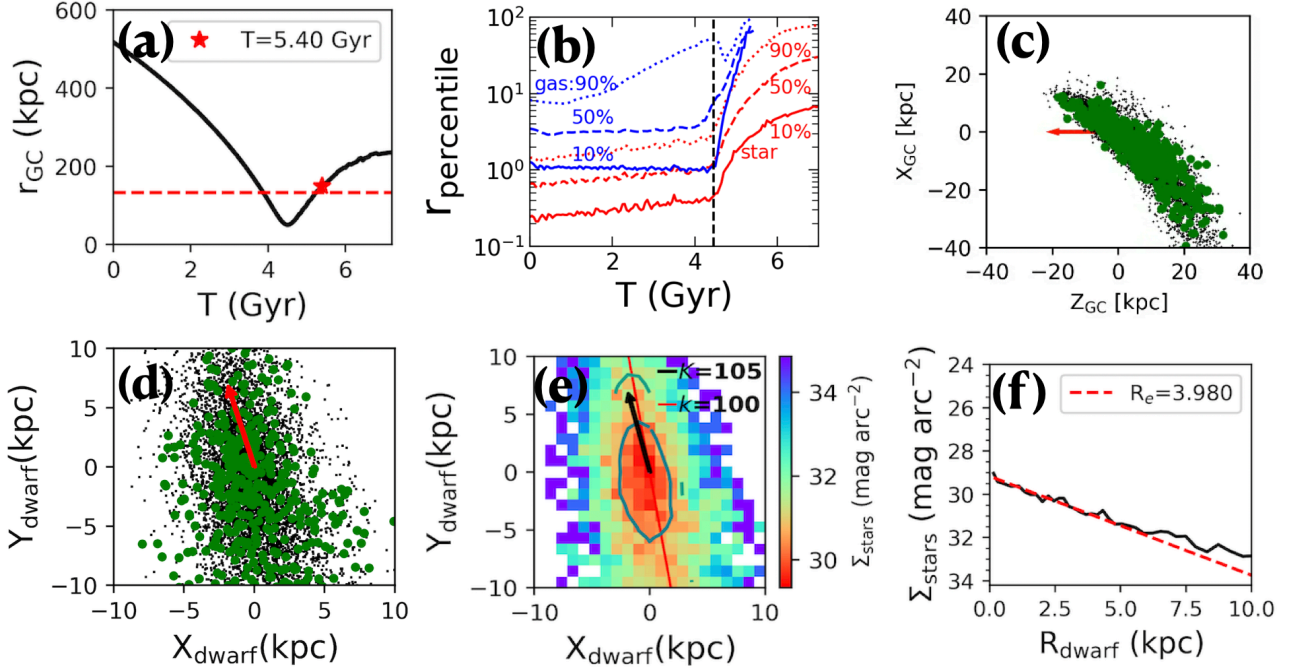


**Figure 5.** Same as Figure 3 but for the Antlia II dwarf. The description of each panel is similar to that of Figure 3 caption.

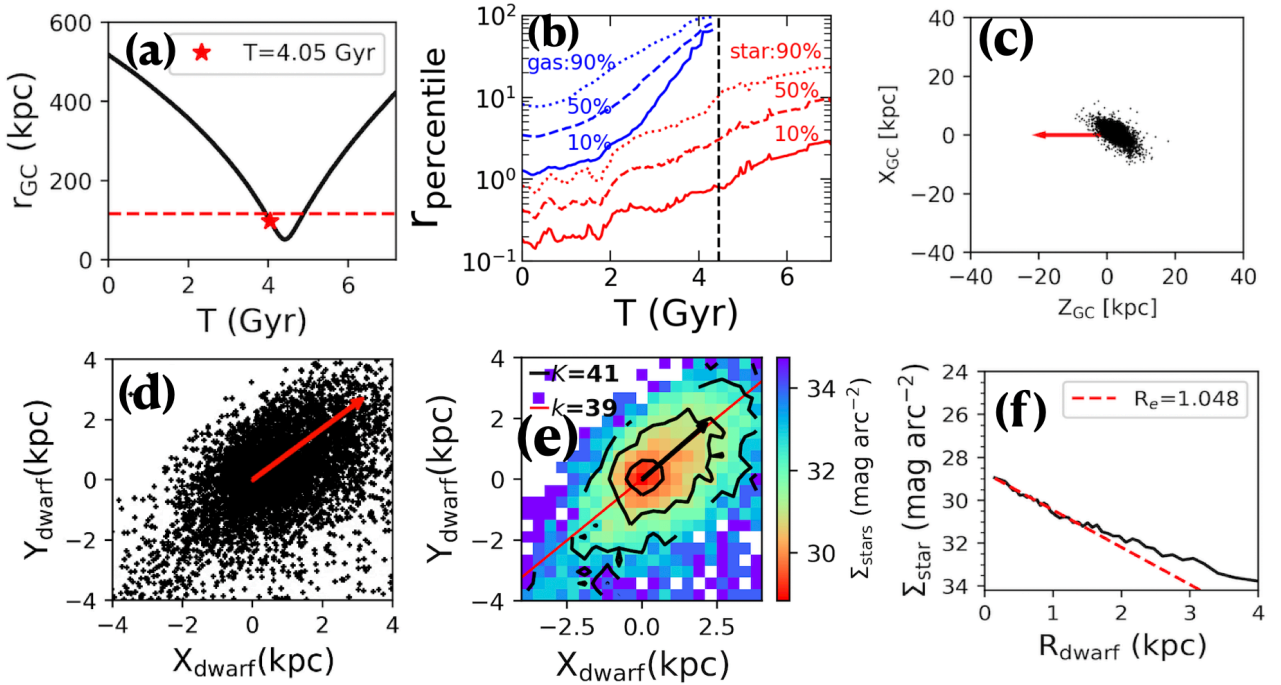


**Figure 6.** Same as Figure 3 but for the Crater II dwarf 4.05 Gyr after the beginning of the simulation. The description of each panel is similar to that of Figure 3 caption.

of an exponential profile as shown in the panel (f). In the latter panel the surface brightness distribution has been calculated after assuming a stellar mass to visible light ratio of 2.5. The fitted total mass is  $\sim 7 \times 10^5 M_{\odot}$ , which can be compared to the observed value of  $3.5 \times 10^5 M_{\odot}$  according to Ji et al. (2021). Observations may have more difficulty to retrieve the total stellar mass of such a faint object when compared to the idealized case of simulations, and we consider that

the simulation result has reached a reasonable agreement with the real Crater II.

Our modeling predicts large amounts of stars distributed in the far dwarf outskirts due to the inflated stellar component in three dimensions. Panel (c) of Figure 6 shows the stellar particle distribution in Galactocentric coordinate system with Z direction pointing to the Galactic center, confirming the expansion in both Z and X direc-

tions. Panel (d) shows the on-sky stellar distribution at large scales, and it confirms the stellar expansion in the X and Y directions. Panel (f) identifies an extra-component beyond 2 kpc in addition to that of the exponential core. This outer faint component may be extremely difficult to be observed as it becomes very faint ( $\Sigma_{\text{stars}} \geq 32 \text{ mag arc}^{-2}$ ), but perhaps future data from *Gaia* may help to retrieve it.

Crater II has not passed its pericenter and given its large distance to the Galactic center, one would not expect strong effects from Galactic tides. This can be seen by comparing panels (c) of Figure 6 to that of Figures 3 and 5, which show much larger (tidal) extents of Sculptor and Antlia II at the faintest levels, in X and Z direction. Panel (e) shows a modest ellipticity of the core contours, which matches pretty well the observations ( $e = 0.12$  from Table 1 of Ji et al. 2021). It is only at the ultra-faint outskirts that the morphology shows an elliptical shape. Simulations show an angle of  $\sim 1.7$  degrees between the core major axis with the proper motion direction, while Ji et al. (2021) found them almost perpendicular. However, given the modest ellipticity found in both observations and simulations, this difference may be not so dramatic.

Both observations and simulations (see fourth row-right panel of Figure 4) show a roughly similar velocity gradient along the major axis with values of  $1.07 \text{ km s}^{-1} \text{ kpc}^{-1}$  and of  $0.7 \text{ km s}^{-1} \text{ kpc}^{-1}$ , respectively. Further fine tuning of the progenitor initial orientation may help to improve the simulation of Crater II, in particular its major axis position angle, which is not well reproduced. For example, we may assume a more elliptical distribution of stars in the progenitor, since the dwarf may have kept a memory of its initial morphology,

The top-right panel of Figure 4 displays the velocity dispersion profile as a function of the projected radius. The blue-solid line gives the measured radial velocity dispersion profile, and the red-dashed line provides the same profile but after removing the velocity gradient. The velocity dispersion (red-dashed line) shows an almost flat dispersion profile with a value of  $\sim 2.5 \text{ km s}^{-1}$ . This low velocity dispersion value is comparable to the observed value ( $2.34 \text{ km s}^{-1}$ , Ji et al. 2021). The stellar mass component contributes only marginally to the velocity dispersion (see the green-dashed line), conversely to the effect of the gas lost and stellar expansion.

The third row-right panel of Figure 4 is based on Eq. 1, i.e., the relation between  $\sigma_{\text{los}}^2/r_{\text{half}}^2$  and the tidal effect strength at pericenter. Objects below the red-dashed line are known to be tidally stripped (e.g., Sgr and Pal 5), which is also the case for both the simulated and the observed Crater II (see third row-right panel of Figure 4 and Figure 5 of Paper II, respectively). This means that Crater II is sufficiently close to pericenter to start being tidally shocked. However, we notice that the properties of the modeled Crater II are discrepant from that observed, especially because panel (a) of Figure 6 shows that the former has a much larger apocenter than the latter ( $r_{\text{apo}} \sim 150 \text{ kpc}$  from Li et al. 2021). Then, conversely to our modeling of Sculptor and Antlia II, we consider that of Crater II to be just an interesting but incomplete attempt.

### 3.5 Numerical convergence and gas removal

Appendix A describes the stability of dwarf progenitors when left in isolation, using the initial conditions displayed in Table 1. It shows that the dwarf core properties are stable, while the outskirts can be affected by effects such as feedback and star formation.

The gas removal process depends on several physical parameters, for example, the orbital pericenter distance, the feedback strength, and also the gas distribution in the progenitors. Dwarfs with smaller pericenter distance would suffer strong ram-pressure stripping and

more efficient gas removal, because the Galactic corona density is larger at smaller radii. Strong feedback also helps to strip the gas (e.g., Hammer et al. 2015). Moreover, the initial gas surface density distribution also affects the gas stripping process, i.e., dwarfs with low gas mass surface density would be more easily stripped.

However, we also have to account for an artificial effect that is linked to the mass ratio between particles of the Galactic corona to that of the dwarf gas (Wang et al. 2019), which likely affects the gas stripping efficiency. Appendix B describes how a large particle mass ratio leads to a more efficient gas stripping. It also indicates that a fine tuning of the above parameters (feedback, gas distribution in dwarfs) allows to recover the reproduction of the dwarfs. However, we underline that parameter values shown in Table 2 may also be slightly dependent on simulation resolution, a problem that hopefully can be solved with much larger resolution in future simulations. For example, Appendix B shows that by improving the resolution by a factor 3, leads us to, e.g., decrease the initial gas mass of the Antlia II progenitor by a factor 1.5, which renders it even more realistic its position in Figure 1.

## 4 DISCUSSION

We propose here that most MW dwarf galaxies have been recently fully transformed during their recent infall into the MW halo (see Papers I and II). During the infall of their gas-rich progenitors, they are affected by physical processes including gas removal from ram pressure of the MW halo gas, a subsequent expansion of stars due to the lack of gravity, and MW tidal shocks occurring near pericenter passage. The scenario is consistent with observations, which is illustrated in Paper I (recent infall from *Gaia* measurements) and Paper II (dependency of their velocity dispersion to orbital parameters). Simulations presented in this paper show that the above processes allow to reproduce many properties (see Table 2) including the excess of velocity dispersion observed in dwarf galaxies, because they are out of equilibrium objects. They also permit to understand why very different kinds of dwarfs can be reproduced by variations within the same set of physical processes. Moreover, simulations allow to characterize the star formation induced by ram pressure, and to predict the fraction of young stars that can be detected, in order to compare them with investigations made in all classical dwarfs (see Yang et al. 2023, submitted, hereafter Paper IV).

### 4.1 Gas turbulence during its removal and tidal shocks increase velocity dispersion

Our dwarf progenitors are fully dominated by the gas component, which imposes very large initial velocity dispersions compared to what would be the contribution of the stellar mass only. It implies that the gas removal leads to a full transformation of the dwarf and of its kinematics. Physical effects are numerous, and they all lead to large values of the line-of-sight velocity dispersion. Immediately after the gas removal, stars expand while keeping their initial (large) velocity dispersion, while the mutual interaction between the gas in the dwarf and in the Galactic corona has created various hydrodynamic phenomena, e.g., shock, compression, or in other words, turbulence. In the meantime, feedback from supernova explosions of the newly formed stars also adds turbulence to the gas, which affects the stellar component until the gas is removed. Gas turbulence may shake the stellar component, providing an additional source for increasing kinetic energy of dwarf stars. Stellar feedback can drive significant kinematic fluctuations of both gas and stars, and this has

been extensively studied by other hydrodynamical simulations of dwarf galaxies (e.g., El-Badry et al. 2016, 2017).

This has to be added to the impact of tidal shocks, which is especially efficient when the dwarf is found near its pericenter (see paper II). Panels (c) of Figures 3, 5, and 6 show the projection of simulated stars along the Z axis, towards the MW. It confirms that star expansion and tidal shocks help to accumulate stars along the Z axis towards the MW, which coincides with that of the MW gravity at pericenter ( $g_{\text{MW}}$ ). According to Paper II (see their Eq. 12) it leads to an increase of the square of the velocity dispersion by  $\Delta\sigma^2$ :

$$\Delta\sigma^2 = 2\sqrt{2}g_{\text{MW}}r_{\text{half}}f_{\text{ff}}, \quad (2)$$

where  $f_{\text{ff}}$  (ff standing for free-fall) represents the fraction of stars that have expanded so much that they are no more affected by the dwarf self-gravity, but by the MW gravity, and it depends also on the structural properties of the dwarf (see details in Paper II). According to Paper II, the relation shown in Eq. 2 between intrinsic parameters and the MW gravity is caused by tidal shocks and gas removal and it leads to a significant correlation shown in their figure 9.

One may also wonder whether or not observers can distinguish between stars at different distances from us. For example, in the simulated Sculptor dwarf more than 90% of stars are within  $\pm 5$  kpc from the core at 83 kpc, according to the second row-left panel of Figure 4. Given the expected accuracy of individual star measurements ( $\sim 20\%$ ), it appears likely that during observational campaigns (Walker et al. 2007, 2009), all stars used to probe kinematics have been selected within that distance range.

## 4.2 Simulations predict outer stellar halos of dwarf galaxies

Recent studies have shown that many dwarfs possess a very extended stellar halo. This includes Tucana II (Chiti et al. 2023), Ursa Minor (Sestito et al. 2023), Bootes I (Longeard et al. 2022), Antlia II (Ji et al. 2021), Fornax (Yang et al. 2022b), Coma Berenices, and Ursa Major (Waller et al. 2023). Although Antlia II shows apparent tidal features, in most other cases, studies have found outskirt stars in all sky directions. Waller et al. (2023) proposed that such stars may have been ejected due to very early and strong feedback. However, Chiti et al. (2023) mentioned that there is no evidence for such an energetic supernova event from their detailed chemical analysis of Tucana II. They suggested a possible early merger, as also proposed by Sestito et al. (2023, see also Goater et al. 2023) for explaining stars found up to 12 half-light radii in the Ursa Minor envelope.

In our scenario, there are two different mechanisms that lead to expand the stellar component. The main channel to explain stars in the outer envelopes of most dwarfs is the (spherical) expansion of the stellar component after gas loss, i.e., due to the subsequent lack of gravity. This mechanism reproduces well the fact that the observed outskirt stars are found in many directions from the dwarf cores (Chiti et al. 2023; Sestito et al. 2023; Longeard et al. 2022; Yang et al. 2022b; Waller et al. 2023). It predicts that stars are expanding in an almost spherical geometry, and without a velocity gradient. Another mechanism is the tidal stretching, which applies well to Antlia II and perhaps also to Crater II (Ji et al. 2021). However, these two dwarfs are very exceptional by their large size associated to their extremely low surface brightness. Together with Sgr, Antlia II and Crater II are the only dwarfs that are clearly dominated by tidal stripping according to their locations in Figure 5 of Paper II.

## 4.3 Star formation history

Gas-rich progenitors of MW dwarf galaxies have their gas content pressurized by the MW halo gas, which predicts some star formation during their infall in the MW halo. Consequently there should be some young stars in MW dwarf galaxies, and especially in the most massive ones. In our simulations, this applies to Sculptor and Antlia II, but not to Crater II because of its very low initial gas surface density (compare the green-dots between panels (d) of Figures 3, 5, and 6). However, the newly formed stars are affected by gas turbulence, especially at the most recent epochs when only small fractions of gas are still attached to the dwarf core.

Turbulent motions lead to quite chaotic motions of recently formed stars, and indeed we find only two stellar particles with young ages ( $\leq 0.5$  Gyr) in the core ( $\leq 2$  kpc) of the simulated Sculptor dwarf. This corresponds to only 0.2% of the Sculptor core stellar mass, which could be compared to observations (see Paper IV).

## 4.4 The difference between Antlia II and Crater II: two extended dwarfs with different velocity dispersions

The major difference between Antlia II and Crater II is related to their different orbital and gas loss histories. Our Crater II progenitor possesses a very low-density gas halo that is removed before the pericenter passage, while the Antlia II gas is removed at pericenter passage. It implies that the kinematics of Antlia II are affected by both gas removal and tidal shocks, as it is observed after pericenter, while those of Crater II are almost exclusively affected by gas removal. This leads to a larger velocity dispersion for Antlia II compared to Crater II, which is also supported by the fact that the former is closer to its pericenter than the latter. Figure 7 shows how Crater II would evolve in the near future, i.e., when arriving at a position close to the pericenter. Panel (a) of Figure 7 shows a much more elongated galaxy than that of panel (d) of Figure 6, i.e., Crater II is likely at an early stage of the tidal stripping (or stretching) process, especially when compared with Antlia II. Panel (b) of Figure 7 also indicates a larger velocity dispersion when compared to the top-right panel of Figure 4.

The above illustrates the roles of the gas removal and tidal shocks at pericenter, which, when combined, are very efficient in increasing the velocity dispersion. However, our simulations show also some limitations especially for reproducing the Crater II properties. While panels (a) of Figures 3, and 5 indicate that both Sculptor and Antlia II become bound to the MW potential, Crater II seems to remain unbound, probably because the gas-removal has been too fast to efficiently slowdown its 3D velocity. It results that while 3D velocities and apocenters of the two first galaxies are well reproduced, the predicted values for Crater II (see Table 2) would require further fine-tuning.

Another interest in comparing Antlia II and Crater II is coming from a recent study by Taibi et al. (2023) showing that most dwarfs belonging to the Vast Polar Structure (VPOS, see Pawlowski et al. 2012) surrounding the MW are found near but before their pericenters. Since Crater II belongs to the VPOS conversely to Antlia II, one may wonder the origin of such a property for most VPOS dwarfs. Comparing panels (b) of Figures 5 and 6 indicates that after the present time, stars of the former are going to expand very rapidly, which might correspond to a full dissolution of the dwarf in the MW halo. One may wonder whether some of the VPOS dwarfs that have passed their pericenter might share a similar fate to that of the Antlia II.



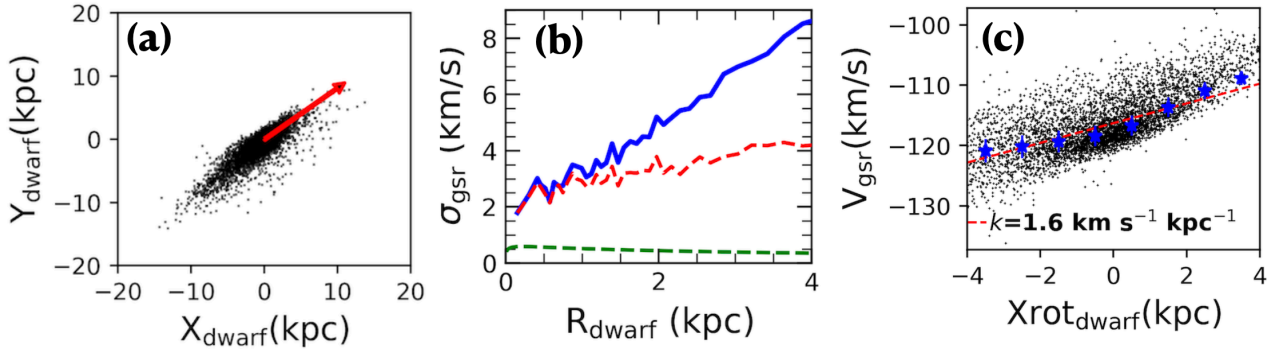


**Figure 7.** The simulated dwarf galaxy Crater II when it will be at pericenter. Panel (a) shows the stellar particle distribution on the sky. Panel (b) shows the velocity dispersion profile in function of the radius. Panel (c) denotes the radial velocity distribution along the major axis.

#### 4.5 The difference between Sculptor and Antlia II: dwarfs with different sizes and with high velocity dispersions

Both Sculptor and Antlia II have lost their gas near pericenter, a position they have both passed recently. Antlia II’s morphology is fully tidally stretched while the Sculptor core does not show significant tidal effects. This is because the core of Sculptor is about 100 times denser than that of Antlia II, as also indicated from the 5 magnitude difference in central surface-brightness. It implies that the former is dense enough to resist the Galactic tides, conversely to the later. This is the reason why Sculptor shows no signature of tides in the central region ( $\sim 2$  kpc). However, at larger scales ( $r \sim 10$  kpc), the model does predict tidal features. Confirming these would require very deep observations.

The above also indicates another possible limitation of our modeling. For example, the top-left panel of Figure 4 shows that in the very central region of Sculptor (within 0.1 kpc) there is a drop of the modeled velocity dispersion, which appears in contradiction with the observations (see the data points). First, this decreasing velocity dispersion in the center may be caused by the artificial softening effect in the numerical simulation. The softening radius for stellar particles is 0.02 kpc, meaning that the central 0.06 kpc is dominated by artificial softening effects. It lets however unexplained the region between 0.06 to 0.1 kpc<sup>4</sup>. Further fine-tuning would be necessary to solve this issue, perhaps by considering a slightly less dense core for Sculptor. A possible alternative might come from observations, since the center of Sculptor may slightly differ from spectroscopic to photometric observations.

## 5 CONCLUSIONS

Analyses of *Gaia* DR3 proper motions have shown that most dwarf galaxies are less bound to the MW than are stars or globular clusters associated to the Gaia-Sausage-Enceladus event and to the infall of the Sgr dwarf system, which have occurred  $9 \pm 1$  and  $5 \pm 1$  Gyr ago, respectively. Paper I found a linear relation between the infall time and the logarithm of the binding energy, which extrapolated to most MW dwarf galaxies, fell in more recently than 3 Gyr ago. During this elapsed time, most dwarf galaxies would not have time to experience more than one orbit, which suggests that they

<sup>4</sup> One may also suspect that because of the expansion of the stellar particles, those seen at 0.1 kpc after the simulation were initially lying in a smaller region and could be also affected by softening effects.

can be at first infall, as has been proposed by Kallivayalil et al. (2013) for the Magellanic Clouds. As a consequence, most dwarf progenitors should have been gas-rich at relatively recent lookback times, because most dwarfs at large distances from a giant spiral in the Local Group are gas rich. It opens the possibility that dwarf progenitors have lost their gas recently near their first passage to pericenter, a location where many dwarfs are currently found (Fritz et al. 2019; Li et al. 2021).

In Paper II, we have shown that pericenter passages are also accompanied by tidal shocks, which lead to correlations between orbital and structural properties of dwarfs. The goal of the present Paper III is to test the above scenario and to verify whether it is consistent with the observed properties of dwarf galaxies. Here, we have considered the complex transformation of gas-rich dwarfs interacting with the MW hot corona (ram pressure) and gravitational field (tides). Simulations have been performed using the GIZMO hydrodynamical solver (Hopkins 2015). There are some limitations for these simulations, which are linked to the different gas particle mass between the MW hot corona and the dwarf galaxy progenitors. This has led us to focus on the specific case of Sculptor, which is massive enough to avoid the above limitations, while it is well representative of classical dwarf spheroidal galaxies.

Hydrodynamical simulations of a gas-rich dwarf galaxy falling into the MW halo have been able to reproduce almost all the observed properties of Sculptor, including its large velocity dispersion when compared to expectations from the gravity due to its sole stellar content. The simulations also succeed to reproduce its core morphology, luminosity profile, velocity gradient, and location in the plane relating structural properties and orbital properties linked to the MW gravitational field. In this scenario, Sculptor’s stellar core can survive the pericenter passage and gas loss, thanks to its sufficiently large density that allows an adiabatic contraction instead of an expansion that affects many stars in the outskirts. This scenario predicts that most MW dwarf galaxies should have lost stars in their outskirts, which are mostly expanding following a spherical symmetry, reproducing observations of stellar halos for many of them (Sestito et al. 2023; Waller et al. 2023; Chiti et al. 2023; Cantu et al. 2021; Yang et al. 2022a; Roederer et al. 2023). However, it also predicts that there should be a tiny fraction of very young stars in Sculptor, for which Paper IV claims their detection.

Using a similar orbital path and more gas-rich progenitors, our simulations have also been able to reproduce the properties of two



unusual dwarf galaxies, Antlia II and Crater II. Their progenitors are rarer than that of Sculptor according to statistical analyses of local field galaxies, which is consistent with the fact that they are both unusual inhabitants of the Galactic halo. Our simulations explain why Antlia II has a much larger velocity dispersion than Crater II, because the former has passed its pericenter and is strongly affected by MW tidal shocks, while the latter is only affected by stellar expansion caused by the lack of gravity after the gas removal.

Here, the proposed scenario of ram-pressure stripping and Galactic tidal shocks has begun to be validated by hydrodynamical simulations, providing considerable changes in our understanding of MW dwarf galaxies. Most of the dwarfs are likely out-of-equilibrium, which prevents any measurements of their mass from assuming self-equilibrium conditions. It also provides an elegant and simple solution for understanding the exceptional behavior of the two extremely low surface brightness dwarfs, Antlia II and Crater II. Finally, further simulations could be useful to verify which fractions the DM could reach while remaining consistent with the transformation in a single pericenter passage of a gas-rich, rotation-dominated dwarfs into a gas-free, dispersion-dominated dwarf as the MW dwarfs are observed to be.

## ACKNOWLEDGMENTS

We are very grateful to Piercarlo Bonifacio, Elisabetta Caffau, Yongjun Jiao, and Hefan Li for their participations to the numerous and lively meetings during which this paper has been discussed. We warmly thank the referee for the very useful remarks, which have considerably help the writing of the manuscript. J.-L.W. acknowledges financial support from the China Scholarship Council (CSC) No.202210740004. Marcel S. Pawlowski acknowledges funding of a Leibniz-Junior Research Group (project number J94/2020). We are grateful for the support of the International Research Program Tian-guan, which is an agreement between the CNRS in France, NAO, IHEP, and the Yunnan Univ. in China.

## DATA AVAILABILITY

The data underlying this article will be shared on request to the corresponding authors.

## REFERENCES

Battaglia G., Helmi A., Tolstoy E., Irwin M., Hill V., Jablonka P., 2008, *ApJL*, **681**, L13  
 Bettinelli M., Hidalgo S. L., Cassisi S., Aparicio A., Piotto G., Valdes F., Walker A. R., 2019, *MNRAS*, **487**, 5862  
 Cantu S. A., et al., 2021, *ApJ*, **916**, 81  
 Cardona-Barrero S., Battaglia G., Nipoti C., Di Cintio A., 2023, *MNRAS*, **522**, 3058  
 Catinella B., et al., 2010, *MNRAS*, **403**, 683  
 Chiti A., et al., 2023, *The Astronomical Journal*, **165**, 55  
 El-Badry K., Wetzel A., Geha M., Hopkins P. F., Kereš D., Chan T. K., Faucher-Giguère C.-A., 2016, *ApJ*, **820**, 131  
 El-Badry K., Wetzel A. R., Geha M., Quataert E., Hopkins P. F., Kereš D., Chan T. K., Faucher-Giguère C.-A., 2017, *ApJ*, **835**, 193  
 Fritz T. K., Battaglia G., Pawlowski M. S., Kallivayalil N., van der Marel R., Sohn S. T., Brook C., Besla G., 2018, *Astronomy and Astrophysics*, **619**, A103  
 Fritz T. K., Carrera R., Battaglia G., Taibi S., 2019, *A&A*, **623**, A129

Gaia Collaboration et al., 2021, *A&A*, **649**, A7  
 Goater A., et al., 2023, *arXiv e-prints*, p. arXiv:2307.05130  
 Grcevich J., Putman M. E., 2009, *ApJ*, **696**, 385  
 Hammer F., Yang Y. B., Flores H., Puech M., Fouquet S., 2015, *ApJ*, **813**, 110  
 Hammer F., Yang Y., Wang J., Arenou F., Puech M., Flores H., Babusiaux C., 2019, *ApJ*, **883**, 171  
 Hammer F., et al., 2023a, *MNRAS*, **519**, 5059  
 Hammer F., et al., 2023b, *arXiv e-prints*, p. arXiv:2311.05677  
 Hayashi K., Hirai Y., Chiba M., Ishiyama T., 2023, *ApJ*, **953**, 185  
 Higgs C. R., McConnachie A. W., Annau N., Irwin M., Battaglia G., Côté P., Lewis G. F., Venn K., 2021, *MNRAS*, **503**, 176  
 Hopkins P. F., 2015, *MNRAS*, **450**, 53  
 Huang S., Haynes M. P., Giovanelli R., Brinchmann J., 2012, *ApJ*, **756**, 113  
 Iorio G., Nipoti C., Battaglia G., Sollima A., 2019, *MNRAS*, **487**, 5692  
 Ji A. P., et al., 2021, *ApJ*, **921**, 32  
 Kalberla P. M. W., Haud U., 2006, *Astronomy & Astrophysics*, **455**, 481  
 Kallivayalil N., van der Marel R. P., Besla G., Anderson J., Alcock C., 2013, *The Astrophysical Journal*, **764**, 161  
 Leisman L., et al., 2021, *AJ*, **162**, 274  
 Lelli F., McGaugh S. S., Schombert J. M., 2016, *AJ*, **152**, 157  
 Li H., Hammer F., Babusiaux C., Pawlowski M. S., Yang Y., Arenou F., Du C., Wang J., 2021, *ApJ*, **916**, 8  
 Longeard N., et al., 2022, *MNRAS*, **516**, 2348  
 Martínez-García A. M., del Pino A., Aparicio A., 2023, *MNRAS*, **518**, 3083  
 Mayer L., 2010, *Advances in Astronomy*, **2010**, 278434  
 Mayer L., Mastrogiuseppe C., Wadsley J., Stadel J., Moore B., 2006, *MNRAS*, **369**, 1021  
 McConnachie A. W., 2012, *AJ*, **144**, 4  
 McConnachie A. W., Venn K. A., 2020, *AJ*, **160**, 124  
 Muñoz R. R., Côté P., Santana F. A., Geha M., Simon J. D., Oyarzún G. A., Stetson P. B., Djorgovski S. G., 2018, *ApJ*, **860**, 66  
 Navarro J. F., Frenk C. S., White S. D. M., 1997, *ApJ*, **490**, 493  
 Nidever D. L., 2014, in Seigar M. S., Treuthardt P., eds, *Astronomical Society of the Pacific Conference Series Vol. 480, Structure and Dynamics of Disk Galaxies*. p. 27 (arXiv:1310.6742)  
 Pace A. B., Erkal D., Li T. S., 2022, *ApJ*, **940**, 136  
 Pawlowski M. S., Pflamm-Altenburg J., Kroupa P., 2012, *MNRAS*, **423**, 1109  
 Putman M. E., Zheng Y., Price-Whelan A. M., Grcevich J., Johnson A. C., Tollerud E., Peek J. E. G., 2021, *ApJ*, **913**, 53  
 Read J. I., Walker M. G., Steger P., 2019, *MNRAS*, **484**, 1401  
 Rocha M., Peter A. H. G., Bullock J., 2012, *MNRAS*, **425**, 231  
 Roederer I. U., Pace A. B., Placco V. M., Caldwell N., Koposov S. E., Mateo M., Olszewski E. W., Walker M. G., 2023, *arXiv e-prints*, p. arXiv:2307.02585  
 Salem M., Besla G., Bryan G., Putman M., van der Marel R. P., Tonnesen S., 2015, *ApJ*, **815**, 77  
 Sestito F., et al., 2023, *arXiv e-prints*, p. arXiv:2301.13214  
 Springel V., 2005, *MNRAS*, **364**, 1105  
 Taibi S., Pawlowski M. S., Khoperskov S., Steinmetz M., Libeskind N. I., 2023, *arXiv e-prints*, p. arXiv:2310.13521  
 Tepper-García T., Bland-Hawthorn J., Pawlowski M. S., Fritz T. K., 2019, *MNRAS*, **488**, 918  
 Torrealba G., Koposov S. E., Belokurov V., Irwin M., 2016, *MNRAS*, **459**, 2370  
 Torrealba G., et al., 2019, *MNRAS*, **488**, 2743  
 Vasiliev E., 2013, *MNRAS*, **434**, 3174  
 Vasiliev E., 2019, *MNRAS*, **482**, 1525  
 Walker M. G., Mateo M., Olszewski E. W., Gnedin O. Y., Wang X., Sen B., Woodroffe M., 2007, *ApJL*, **667**, L53  
 Walker M. G., Mateo M., Olszewski E. W., Peñarrubia J., Evans N. W., Gilmore G., 2009, *ApJ*, **704**, 1274  
 Waller F., et al., 2023, *MNRAS*, **519**, 1349  
 Wang J., Hammer F., Yang Y., Rippepi V., Cioni M.-R. L., Puech M., Flores H., 2019, *MNRAS*, **486**, 5907  
 Wang J., Hammer F., Yang Y., 2022, *MNRAS*, **515**, 940

- Westfall K. B., Majewski S. R., Ostheimer J. C., Frinchaboy P. M., Kunkel W. E., Patterson R. J., Link R., 2006, *The Astronomical Journal*, **131**, 375
- Wolf J., Martinez G. D., Bullock J. S., Kaplinghat M., Geha M., Muñoz R. R., Simon J. D., Avedo F. F., 2010, *MNRAS*, **406**, 1220
- Yang Y., Hammer F., Fouquet S., Flores H., Puech M., Pawlowski M. S., Kroupa P., 2014, *MNRAS*, **442**, 2419
- Yang Y., Ianjamasimanana R., Hammer F., Higgs C., Namumba B., Carignan C., Józsa G. I. G., McConnachie A. W., 2022a, arXiv e-prints, p. arXiv:2204.03662
- Yang Y., Hammer F., Jiao Y., Pawlowski M. S., 2022b, *MNRAS*, **512**, 4171
- de Boer T. J. L., et al., 2012, *A&A*, **539**, A103

## APPENDIX A: STABILITY OF INITIAL CONDITIONS FOR THE DWARF PROGENITORS

Figure A1 shows the evolution of the projected surface brightness and line-of-sight velocity dispersion for the progenitors of the three dwarfs assumed to be in isolation for 2 Gyr. In order to calculate the surface brightness, we have assumed their distance to be 517 kpc (the starting position of simulation models). The high surface mass density of gas and high feedback strength used in Sculptor lead to relatively large variations in surface brightness at large radii. This variation is caused by the strong adopted feedback and star formation, which result in large variations at the outskirts, i.e., beyond 4 times the half-light radius. The low gas mass for Crater II and median feedback strength for Antlia II lead to relatively stable surface brightness and velocity dispersion profile. However, for all gas-rich dwarf progenitors the velocity dispersion does not change by more than  $2\text{--}3\text{ km s}^{-1}$ , and it always shows a relatively flat profile. The effect of gas perturbation onto stars are much more effective when the dwarfs fall into the Galactic corona. This is because hydrodynamical processes such as ram-pressure, tidal shocks, and turbulence, make the stellar component much more perturbed by turbulence during the time the dwarf progenitors are dominated by the gas interacting with the Galactic coronae.

## APPENDIX B: RESOLUTION DEPENDENCY OF PARAMETERS TO REPRODUCE DWARF PROPERTIES

Ideally, it would be better to use the same resolution for gas particles of the Galactic corona and of the dwarf progenitors. But this is too expensive in calculation time because the dwarfs are too tiny when compared to the Milky Way. It would require 10, 15 and 30 times more particles for Milky Way model than what has been used in our current modeling with  $\sim 30$  million particles. Simulations with such high numbers of particles are not feasible currently. Therefore, we have used lower resolution modeling in our current work to investigate the parameter space, and to search for the best matched dwarf modeling. However, we have tested the impact of resolution by increasing by a factor 3 the number of particles of the Milky Way halo gas. We have found that it leads to larger elapsed times (by about one Gyr) for dwarf progenitors to be fully gas-stripped.

Figure B1 shows how one may need to reinvestigate the parameter space for matching observations after performing higher resolution simulations. This illustrates the interplay between these parameters and the resolution of the MW gas particles in the simulation.

For Crater II, increasing the MW particle resolution by a factor 3 results in gas removal at  $\sim 4.35$  Gyr (and a distance of 102 kpc), compared to  $\sim 3.4$  Gyr in the fiducial simulation. However, the velocity dispersion profile is similar to the low resolution one (see

left panel of Figure B1). For the Antlia II simulation, increasing the MW particle resolution also delays the gas stripping. We find that by decreasing the initial gas fraction by a factor of 1.5, the gas can be stripped near pericenter, and the observed velocity dispersion is rather well recovered (see right panel of Figure B1) as it was in the low resolution simulation (see Figure 5). Nevertheless, Figure B1 shows that one may recover the observed properties of dwarfs at higher numerical resolutions.

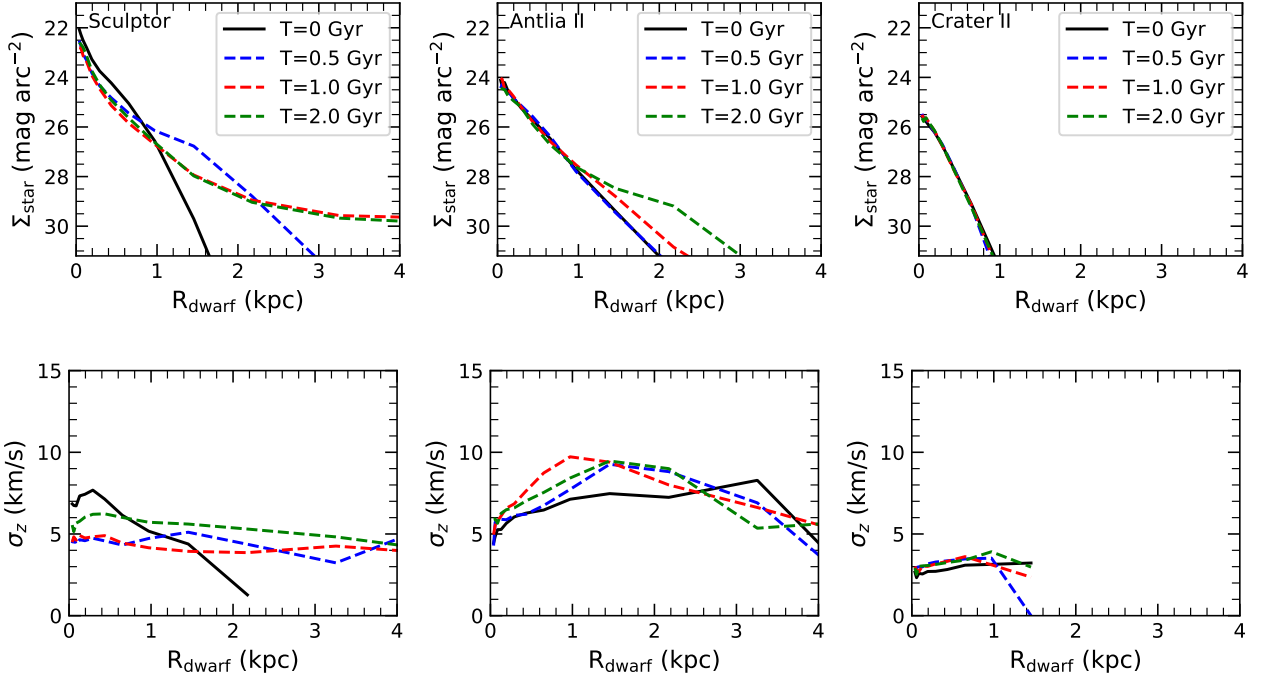


**Figure A1.** Evolution of the surface brightness and projected velocity dispersion profiles for the dwarf progenitors assumed to be in isolation.

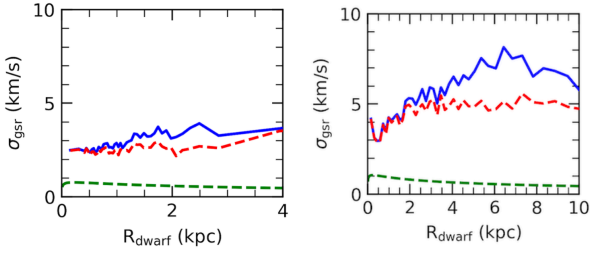


**Figure B1.** Velocity dispersion profiles for Crater II (left panel) and Antlia II (right panel) with a higher resolution for the MW gas particles. Increasing resolution of Galactic model leads to delaying the gas stripping. By tuning other parameters, we can strip the gas of dwarf at slightly different observation times. For the Crater II analog, the time delay does not change the velocity dispersion too much. For Antlia II, decreasing the gas fraction by a factor of 1.5 shortens the gas stripping time, allowing it to occur near pericenter. The velocity dispersion is roughly recovered as it is shown in the right panel.